Journal of Electrical Bioimpedance
www.bioimpedance.net

J Electr Bioimp, vol. 2, pp. 33–47, 2011
Received: 30 Mar 2011, published: 15 Jun 2011
doi:10.5617/jeb.170

# Improving Conductivity Image Quality Using Block Matrix-based Multiple Regularization (BMMR) Technique in EIT: A Simulation Study

Tushar Kanti Bera[1], Samir Kumar Biswas[2], K. Rajan[2], J. Nagaraju[1]

1. *Department of Instrumentation and Applied Physics, Indian Institute of Science, Bangalore-560012, INDIA*
2. *Department of Physics, Indian Institute of Science, Bangalore-560012, INDIA*
3. *E-mail any correspondence to: solarjnr@isu.iisc.ernet.in*

**Abstract**
A Block Matrix based Multiple Regularization (BMMR) technique is proposed for improving conductivity image quality in Electrical Impedance Tomography (EIT). The response matrix ($J^TJ$) has been partitioned into several sub-block matrices and the largest element of each sub-block matrix has been chosen as regularization parameter for the nodes contained by that sub-block. Simulated boundary data are generated for circular domains with circular inhomogeneities of different geometry and the conductivity images are reconstructed in a Model Based Iterative Image Reconstruction (MoBIIR) algorithm. Conductivity images are reconstructed with BMMR technique and the results are compared with the Single-step Tikhonov Regularization (STR) and modified Levenberg-Marquardt Regularization (LMR) methods. Results show that the BMMR technique improves the impedance image and its spatial resolution for single and multiple inhomogeneity phantoms of different geometries. It is observed that the BMMR technique reduces the projection error as well as the solution error and improves the conductivity reconstruction in EIT. Results also show that the BMMR method improves the image contrast and inhomogeneity conductivity profile by reducing background noise for all the phantom configurations.

**Keywords:** EIT, MoBIIR, Jacobian, Block Matrix-based Multiple Regularization (BMMR), simulated boundary data, conductivity imaging, STR, LMR, normalized projection error, normalized solution error.

## Introduction

Electrical Impedance Tomography (EIT) [1-4] is a computed tomographic technique in which the electrical conductivity or resistivity distribution in a closed domain ($\Omega$) is reconstructed from the boundary potentials developed by a constant current signal injected at the domain boundary ($\partial\Omega$) (Fig.-1). EIT has been researched extensively in medical diagnosis [5-11] and other fields of science and engineering [12-15] due to its number of advantages [16-18]. A practical EIT system has, generally, poor signal to noise ratio [19] and poor spatial resolution [20] due to the factors associated with it. The boundary data profile [21] of the practical phantom [22-26] is highly sensitive to modeling parameters [27] such as the phantom structure [23, 26], surface electrodes geometry [21], experimental errors [23, 26, 28] and errors of the EIT-instrumentation [29-32]. That is why there are a number of opportunities and challenges in EIT to make this technology as an efficient medical imaging modality like other popular tomographic techniques available [33] by improving its image quality. Reconstructed image quality depends on the boundary data error and the performance of the reconstruction algorithm. The performance of the reconstruction algorithm again depends on the Jacobian matrix (J), response matrix ($J^TJ$), regularization technique used and the regularization parameter ($\lambda$).

EIT is a nonlinear ill-posed inverse problem [27] in which a small amount of noise in the boundary measurement data can lead to enormous errors in the estimates. Regularization techniques [27, 34-35] are, generally, incorporated in the reconstruction algorithm to constrain its solution domain by making the problem well-posed. Hence the image quality in EIT greatly depends on the regularization technique and the regularization parameter ($\lambda$) used in the reconstruction algorithm. The regularization parameter ($\lambda$) in Single-step Tikhonov regularization (STR) [27] is taken as a constant value along the diagonal elements of the response matrix $J^TJ$. On the other hand, in the Levenberg-Marquardt regularization (LMR) [36] method, $\lambda$ is taken as the largest element of the response matrix $J^TJ$ ($\max(\max(J^TJ))$) or any other suitable constant real number and then it is gradually decreased by a factor of $\sqrt{10}$ or any other suitable constant from iteration to iteration. Hence, in the STR and LMR methods, the regularization parameter is set as a small constant number in all the iterations of the reconstruction process. Thus the regularization effect remains the same all over the domain (for all the nodal positions). As a result, the local or regional physiological attributes of the domain under test are not taken into account in the STR and LMR methods.

In this paper, the local physiological information is preserved through the multiple regularization process which is then integrated to the ill-posed inverse problem to make the regularization more effective and optimum for the whole domain. In this direction a regional block matrix based multiple regularization (BMMR) method [37] is proposed for EIT. The BMMR regularization technique preserves the spatial information over the domain and gives contrast regularization along the diagonal nodes of the

system matrix. The BMMR method is integrated in a Model Based Iterative Image Reconstruction (MoBIIR) algorithm [38] developed and the impedance image reconstruction is studied using simulated data. Conductivity images are reconstructed for different phantom configurations using the BMMR technique and the results are compared with the STR and LMR methods.

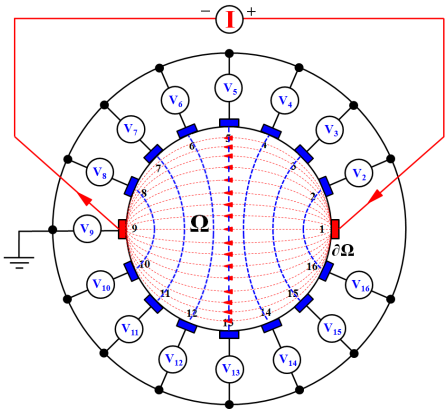


Fig.1: Current injection and voltage measurement in EIT for a closed domain (Ω) surrounded by surface electrodes at the domain boundary (∂Ω) (red and blue electrode represent the current and voltage electrodes respectively).

## Materials and methods

*Regularized Reconstruction in EIT*

For a low frequency (<100 kHz) sinusoidal constant current injection at the boundary ($\partial\Omega$) of a closed domain ($\Omega$) containing a homogeneous and isotropic medium with low magnetic permeability (biological tissue) and electrical conductivity ($\sigma$), the electrical potential ($\Phi$) developed at a point P (P = P (x, y) in Cartesian coordinate system) within $\Omega$ can be represented as [4, 18, 39-40]:

$$\nabla \bullet \sigma(x,y)\nabla\Phi(x,y) = 0 \qquad (1)$$

where $\nabla$ is the gradient operator in the system.

This nonlinear partial differential equation relating the conductivity to the potential in the closed domain (volume conductor) under test is known as the Governing Equation of EIT [4, 18, 39-40] and has an infinite number of solutions. Boundary conditions [4, 18, 39-40] are applied to restrict the solutions of the Eq.-1 which may be either the Dirichlet type or the Neumann type or a mixture of the previous two. Due to the insufficient known variables and the inherent ill-posedness of the system, direct analytical methods fail to get the unique solution of this problem and hence a minimization algorithm [39-41] is found as the best way to obtain its approximate solution. In the minimization algorithm, an objective function, formed by the difference between the experimental or measured data ($V_m$) and the model predicted data ($V_c$), is minimized by the Gauss-Newton method [39-43] to find the approximate solution.

Conductivity reconstruction in EIT is a nonlinear, highly ill-posed [39-43] inverse problem in which a small amount of noise in the boundary data can lead to enormous errors in the estimates. Hence, EIT needs a regularization technique [39-43] with a suitable regularization parameter ($\lambda$) to constrain its solution space as well as to convert the ill-posed problem into a well-posed one. A regularized solution of the inverse problem not only decreases the ill-posed characteristics of the inverse matrix but also, it improves the reconstructed image quality.

Considering $\mathbf{V_m}$ as the measured voltage matrix and **f** as a function mapping an E-dimensional (E is the number of elements in the finite element mesh [44]) impedance distribution into a set of M (number of the measured data available) measured voltage data, an object function can be defined as the L-2 norm of the difference between $V_m$ and f [39-43]:

$$s_r = \frac{1}{2}\left\| V_m - f \right\|^2 + \frac{1}{2}\lambda_r \left\| G\sigma \right\|^2 \qquad (2)$$

where $\mathbf{s_r}$ is the constrained least-square error of the reconstruction, **G** is the regularization matrix and $\boldsymbol{\lambda_r}$ is a positive scalar called as the regularization coefficient or regularization parameter.

By the Gauss Newton (GN) method the conductivity update vector [$\Delta\sigma$] is given by:

$$\Delta\sigma = -\frac{\frac{d}{d\sigma}(s_r)}{\frac{d^2}{d\sigma^2}(s_r)} = \frac{(f')^T(V_m - f) - \lambda_r (G)^T (G\sigma)}{(f')^T(f') - (f'')^T(V_m - f) + \lambda_r G^T G} \qquad (3)$$

Neglecting higher terms and replacing $\mathbf{f'}$ by **J** and $\mathbf{G^TG}$ by **I** (Identity matrix), the update vector reduces to

$$\Delta\sigma = \left(J^T J + \lambda_r I\right)^{-1}\left(J^T\left(V_m - f\right) - \lambda_r I\sigma\right) \qquad (4)$$

where the term $\mathbf{f' = J}$ is known as the Jacobian matrix of dimension (g × h) and is defined by [39-41]:

$$J = [f']_{gh} = \frac{\partial f_g}{\partial \sigma_h} \qquad (5)$$

Hence, the Gauss-Newton approach gives a general solution of the conductivity distribution for the $k^{th}$ iteration as:

$$\sigma_{k+1} = \sigma_k + \left(J^T J + \lambda_r I\right)^{-1}\left(J^T\left(V_m - f\right) - \lambda_r I\sigma_k\right) \qquad (6)$$

*MoBIIR Algorithm*

In the MoBIIR algorithm, a forward model based iterative image reconstruction approach based on linear perturbation equation is followed. The linear perturbation equations containing the first derivative of the forward operator are derived from the EIT governing equation (Eq.-1). It is then solved to calculate the boundary potential for known current conduction and conductivity using the finite element method (FEM) [45]. The solution of the forward problem is also used to compute the Jacobian (**J**) by adjoint method [46] using the Eq.-7:

$$J = \oint_{\Omega} \nabla U_s . \nabla U_d \, d\Omega \tag{7}$$

where $U_s$ is the forward solution for a particular source location and $U_d$ is the forward solution for the adjoint source location (source at the detector location and detector at the source location). The simultaneous equation is solved using conjugate gradient search to obtain the update vector for electrical conductivities [$\mathbf{\Delta\sigma}$].

The perturbation equation is updated by recomputing the first derivative after each update of the electrical conductivities.

The MoBIIR algorithm starts with the forward solution of the EIT governing equation (Eq.-1) to calculate the boundary potential matrix [$\mathbf{V_c}$] for a known current injection matrix [**C**] and a known (initial guess) conductivity matrix [$\mathbf{\sigma_0}$]. In the approximation algorithm a least square solution of the minimized object function ($\mathbf{s_r}$) is obtained which gives an estimation of a potential $\mathbf{V_c}$ from which $\mathbf{\Delta V}$ ($\mathbf{\Delta V = V_m - V_c}$) is estimated for the next iterations. The voltage difference matrix [$\mathbf{\Delta V = V_m - V_c}$] is estimated and then it is used to calculate the conductivity update matrix [$\mathbf{\Delta\sigma}$] using the Eq.-4. [$\mathbf{\Delta\sigma}$] is used to improve the [$\mathbf{\sigma_o}$] matrix a to new conductivity matrix [$\mathbf{\sigma_1 = \sigma_o + \Delta\sigma}$] (as shown in Eq.-6). In the second iteration, [$\mathbf{\sigma_1}$] is used to calculate a new boundary voltage matrix and a new update vector [$\mathbf{\Delta\sigma_1}$]. The [$\mathbf{\Delta\sigma_1}$] matrix is then used to update the [$\mathbf{\sigma_1}$] for obtaining a new conductivity matrix [$\mathbf{\sigma_2}$]. In this way at the ($\mathbf{k^{th}}$) iteration, the update vector becomes [$\mathbf{\Delta\sigma_k}$] and the conductivity matrix becomes [$\mathbf{\sigma_{k+1} = \sigma_k + \Delta\sigma_k}$].

*Block Matrix based Multiple Regularization (BMMR)*

The measurement data for each projection in EIT can be written in the form of following system of equations:

$$\begin{array}{ccccccccccccc}
a^1_{11}x_1 & + & a^1_{12}x_2 & + & \cdot & \cdot & \cdot & + & a^1_{1(N-1)}x_{N-1} & + & a^1_{1N}x_N & = & b^1 \\
a^2_{21}x_1 & + & a^2_{22}x_2 & + & \cdot & \cdot & \cdot & + & a^2_{2(N-1)}x_{N-1} & + & a^2_{2N}x_N & = & b^2 \\
\cdot & & \cdot & & \cdot & \cdot & \cdot & & \cdot & & \cdot & = & \cdot \\
\cdot & & \cdot & & \cdot & \cdot & \cdot & & \cdot & & \cdot & = & \cdot \\
\cdot & & \cdot & & \cdot & \cdot & \cdot & & \cdot & & \cdot & = & \cdot \\
a^{m-1}_{(N-1)1}x_1 & + & a^{m-1}_{(N-1)2}x_2 & + & \cdot & \cdot & \cdot & + & a^{m-1}_{(N-1)(N-1)}x_{N-1} & + & a^{m-1}_{(N-1)N}x_N & = & b^{m-1} \\
a^1_{N1}x_1 & + & a^m_{N2}x_2 & + & \cdot & \cdot & \cdot & + & a^m_{N(N-1)}x_{N-1} & + & a^m_{NN}x_N & = & b^m
\end{array} \quad \text{---- (8)}$$

where N is the number of nodes in the finite element mesh, $x_i$ (i = 1, 2, 3, …, N) is the conductivity at the corresponding nodes, $a_{ij}$ is the coefficient of the $x_i$ (conductivity) at each node and $\mathbf{b^m}$ (m = 1, 2, 3, …, M) is the corresponding nodal potentials and M is the number of boundary measurements available. From the Gauss-Newton method (without incorporating the regularization technique) the normal equation [47] can be written as:

$$[A]_{N\times N}[x]_{N\times 1} = [B]_{N\times 1} \tag{9}$$

where,

$$[A]_{N\times N} = [J^T]_{N\times M}[J]_{M\times N} \tag{10}$$

and,

$$[B]_{N\times 1} = [J^T]_{N\times M}[b]_{M\times 1} \tag{11}$$

Hence, for EIT, Eq.-8 reduces to:

$$[J^T]_{N\times M}[J]_{M\times N}[\Delta\sigma]_{N\times 1} = [J^T]_{N\times M}[\Delta V]_{M\times 1} \tag{12}$$

To make the ill-posed problem well-posed, a regularization term $\mathbf{\lambda I}$ is added to the matrix **A** (or $\mathbf{J^TJ}$), where **I** is an identity matrix and $\mathbf{\lambda}$ is called the regularization parameter. In this context a block matrix based multiple regularization method is proposed which calculates the multiple regularization parameters from the system response matrix [$\mathbf{J^TJ}$] and form a new response matrix called BMMR matrix ($[\mathbf{Z_{BMMR}}]_{N\times N}$) within each of the inner iterations of Conjugate Gradient Search (CGS). The matrix $[\mathbf{Z_{BMMR}}]_{N\times N}$ is formed with the diagonal matrices $[\mathbf{W_i}]_{n\times n}$ ($n=\sqrt{N}$) containing all the diagonal elements equal to the largest element ($\mathbf{\eta_i}$) of the adjoint matrices (of their corresponding positions) of [$\mathbf{J^TJ}$].

The response matrix $J^TJ$ is rearranged by separating all the adjoint matrices ($[L_{pq}]_{n\times n}$: p, q = 1, 2, 3, …, n) and a matrix **A** is formed as (Fig.-2a):

$$A = [[L_{pq}]_{n\times n}]_{N\times N} \tag{13}$$

where, $n=\sqrt{N}$

If the matrix **A** is further reformed as:

$$L_{pq} = [a_{ij}]_{n\times n} \text{ when, } p = q$$
$$L_{pq} = \text{Null Matrix, when, } p \neq q$$

Then, the matrix **A** is reduces to **Y** given by (Fig.-2b):

$$[Y]=\begin{bmatrix} [L_{11}]_{n\times n} & [\Phi]_{n\times n} & [\Phi]_{n\times n} & \cdots & [\Phi]_{n\times n} & [\Phi]_{n\times n} \\ [\Phi]_{n\times n} & [L_{22}]_{n\times n} & [\Phi]_{n\times n} & \cdots & [\Phi]_{n\times n} & [\Phi]_{n\times n} \\ [\Phi]_{n\times n} & [\Phi]_{n\times n} & [L_{33}]_{n\times n} & \cdots & [\Phi]_{n\times n} & [\Phi]_{n\times n} \\ \vdots & \vdots & \vdots & \ddots & \vdots & \vdots \\ [\Phi]_{n\times n} & [\Phi]_{n\times n} & [\Phi]_{n\times n} & \cdots & [L_{(n-1)(n-1)}]_{n\times n} & [\Phi]_{n\times n} \\ [\Phi]_{n\times n} & [\Phi]_{n\times n} & [\Phi]_{n\times n} & \cdots & [\Phi]_{n\times n} & [L_{nn}]_{n\times n} \end{bmatrix}_{N\times N}$$

---- (14)

where, $[\Phi]_{n\times n}$ is a null matrix given by:

$$[\Phi]_{n\times n} = [a_{ij}]_{n\times n} \qquad (15)$$

Where $a_{ij} = 0$ for all i and j.

Now the maximum values ($\eta_i$: i=1, 2, 3, …, n) of all the block matrices ($\mathbf{L_{ii}}$) are calculated as:

$$\eta_i = \max(\max([L_{ii}])) \qquad (16)$$

Using $\eta_i$, n diagonal matrices ($[\mathbf{W_i}]$: i=1, 2, 3, …, n) are formed in which all the diagonal elements of $[\mathbf{W_i}]$ are $\eta_i$ and all the other elements are set as zero. Hence the $[\mathbf{W_i}]$ matrices are defined as:

$$[W_i]_{n\times n} = \begin{bmatrix} \eta_i & 0 & 0 & \cdots & 0 & 0 \\ 0 & \eta_i & 0 & \cdots & 0 & 0 \\ 0 & 0 & \eta_i & \cdots & 0 & 0 \\ \vdots & \vdots & \vdots & \ddots & \vdots & \vdots \\ 0 & 0 & 0 & \cdots & \eta_i & 0 \\ 0 & 0 & 0 & \cdots & 0 & \eta_i \end{bmatrix}_{n\times n} \qquad (17)$$

Replacing all the diagonal adjoint block matrices ($[\mathbf{L_{ii}}]$: i = 1, 2, 3, …, n) by newly formed diagonal matrices $[\mathbf{W_i}]$ in matrix $[\mathbf{Y}]$, a matrix $[\mathbf{Z_{BMMR}}]$ called the BMMR matrix is formed as:

$$[Z_{BMMR}]=\begin{bmatrix} [W_1]_{n\times n} & & & & & & \\ & [W_2]_{n\times n} & & & & & \\ & & [W_3]_{n\times n} & & & & \\ & & & \ddots & & & \\ & & & & [W_i]_{n\times n} & & \\ & & & & & [W_{n-1}]_{n\times n} & \\ & & & & & & [W_n]_{n\times n} \end{bmatrix}_{N\times N}$$

---- (18)

Hence, the diagonal elements (nonzero elements) in the matrix $[\mathbf{Z_{BMMR}}]$ are arranged in the following manner as shown as the schematic of the BMMR matrix (Fig.-2c). Therefore the expression of the conductivity update vector with BMMR technique reduces to:

$$\sigma_{k+1} = \sigma_k + \left(J^T J + \lambda Z_{BMMR}\right)^{-1}\left(J^T(V_m - f) - \lambda Z_{BMMR}\sigma_k\right) \qquad (19)$$

The BMMR matrix incorporates the information produced by the local physiological changes in the system which is generally overshadowed in the STR or LMR method.

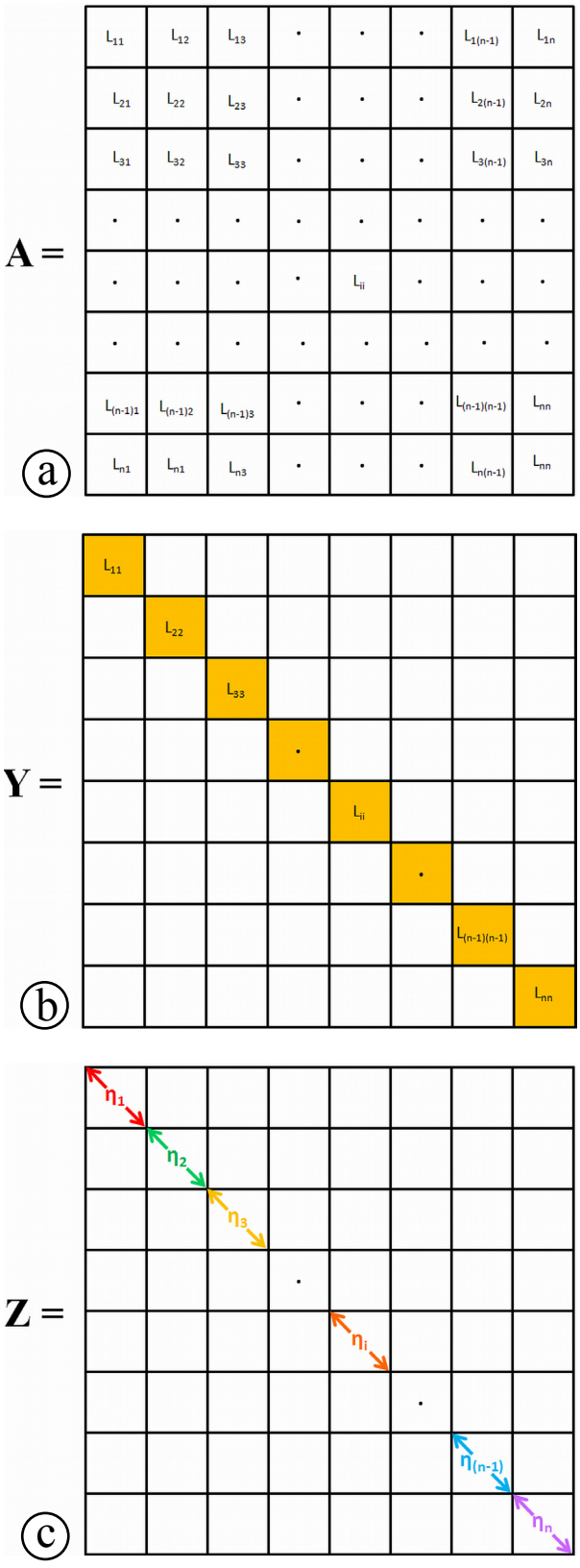


Fig.2: BMMR matrix formation: (a) A matrix formation by defining several block matrices in $J^TJ$ matrix, (b) Y matrix formation from A matrix, (c) BMMR matrix or Z matrix formation from Y matrix.

In the MoBIIR algorithm with STR regularization, a constant regularization parameter ($\lambda_r = \lambda * \eta$) is used where the $\eta$ is a constant calculated as the largest element of the response matrix $J^TJ$ ($\max(\max(J^TJ))$). Hence, in the STR method, the $\lambda_r$ remains unchanged for all the iterations. On the other hand, in the MoBIIR with LMR method, $\eta$ is taken as the largest element of the response matrix $J^TJ$ to form the $\lambda_r$ ($\lambda_r = \lambda * \eta$) in the first iteration. But for all the other iterations, $\lambda_r$ is gradually decreased by a factor of $\sqrt{10}$. Hence, in both the STR and LMR methods, the regularization parameter ($\lambda_r$) remains a small constant number suitably calculated (as stated above) from the response matrix ($J^TJ$) in each of the iterations of the reconstruction process. Therefore, the local or regional physiological information of the nodal points in the domain under imaging are not taken into account in the STR and LMR methods. Hence, in both the STR and LMR methods, a constant regularization parameter is being used at each iteration and as a result the local or regional physiological attributes are not taken into account in them. Furthermore, due to the addition of constant regularization parameter to the matrix **A**, it perturbs the original system of equations and these perturbations are not based on the spectral information. Hence this perturbation may introduce a significant error in the solution as well as some unwanted solution could be obtained.

For the entire study, a symmetric finite element mesh containing 512 triangular elements and 289 nodes is used in the MoBIIR both for the forward and inverse solution of the image reconstruction process.

*Image Reconstruction with Simulated Boundary Data*

Boundary potential data are generated by simulating a constant current (1 mA) injected to a circular phantom (Diameter ($D_p$) = 150 mm) with circular inhomogeneity with a conductivity of 0.02 S/m surrounded by a homogeneous background medium (conductivity = 0.58 S/m). Boundary data are generated with a number of phantom geometries simulated with circular inhomogeneities of different diameters (D) and situated at different distances (center to center distance, L) from the phantom center. Conductivity images are reconstructed from all the boundary data in the MoBIIR with BMMR regularization technique and the results are compared with the STR and LMR methods. All the images are analyzed with their contrast parameters defined by their elemental conductivity profiles.

*Image Analysis with Contrast Parameters and Normalized Error Terms*

Contrast to noise ratio (CNR) [48], percentage of contrast recovery (PCR) [48], coefficient of contrast (COC) [48] and mean inhomogeneity conductivity ($IC_{Mean}$) are calculated for the images reconstructed by all the regularization techniques and regularization parameters to compare the reconstruction accuracy. To further analyze the proposed method, normalized projection error (error due to the voltage mismatch), $E_V$ [48] and the normalized solution error norm ($E_\sigma$) [48] are also calculated in the STR, LMR and BMMR methods for all the iterations with different values of $\lambda$. $E_V$ and $E_\sigma$ are calculated in each iteration as:

$$E_V = \frac{1}{2}\left\|V_m - V_c\right\|^2 \tag{21}$$

$$E_\sigma = \frac{\left\|\sigma_{reconstructed} - \sigma_{true}\right\|}{\left\|\sigma_{true}\right\|} \tag{22}$$

**Results**

It is observed that the projection errors ($E_V$) in STR and LMR becomes minimum at $\lambda$ = 0.0001 (Fig.-3a) and $\lambda$ = 0.0001 (Fig.-3b), respectively. However, in the BMMR method the $E_V$ becomes minimum at $\lambda$ = 0.01 (Fig.-3c).

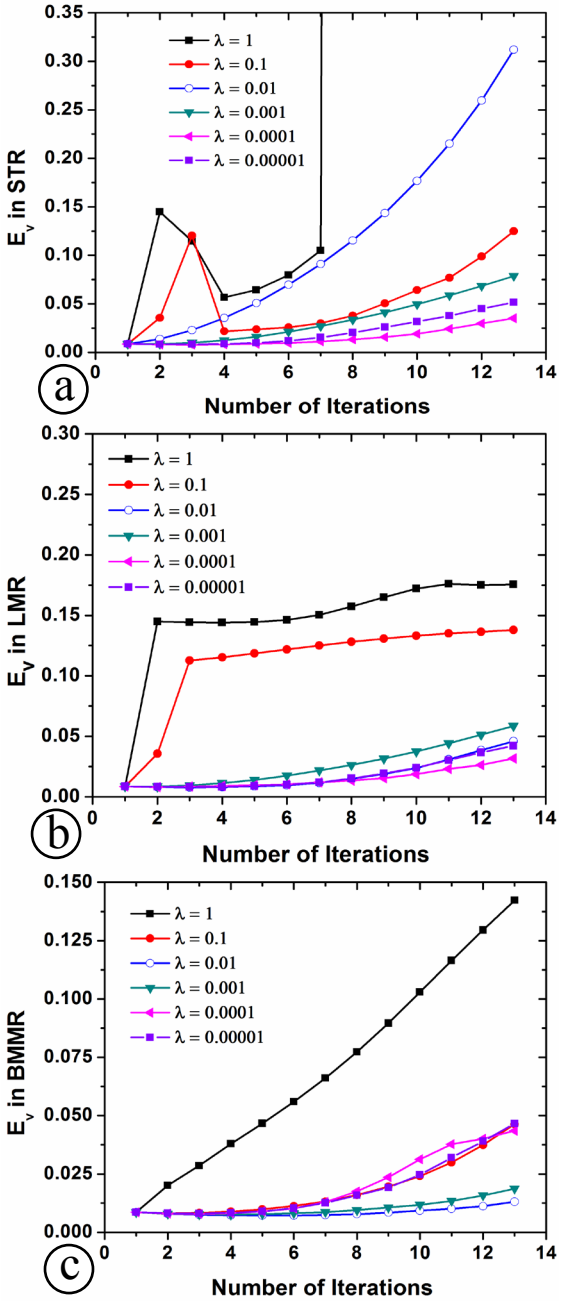


Fig.3: Projection errors ($E_V$) calculated in the conductivity reconstruction at different iterations with different values of $\lambda$: (a) with STR, (b) with LMR, (c) with BMMR.

Conductivity reconstructions show that the $E_V$ (Fig.-4a) and the $E_\sigma$ (Fig.-4b) in STR and LMR are larger than in the BMMR technique.

To compare the image reconstruction and image quality in the STR, LMR and BMMR methods, the conductivity reconstruction is conducted first with $\lambda = 0.01$ and then with $\lambda = 0.0001$. For further study, the conductivity reconstruction is also conducted with an intermediate value of $\lambda$ (with $\lambda = 0.00011$ and $\lambda = 0.0011$). Imaging with $\lambda = 0.0001$ in all the methods (STR, LMR and BMMR) gives a more clear aspect of the proposed method (BMMR) as STR and LMR methods show the best result at $\lambda = 0.0001$. The conductivity images are also reconstructed for the phantoms with inhomogeneities of different diameters and different geometric positions using the STR, LMR and BMMR methods with different values of $\lambda$. $= 0.0001$. Conductivity imaging is also studied with single, double and triple inhomogeneity phantoms with the STR, LMR and BMMR methods and the results are compared.

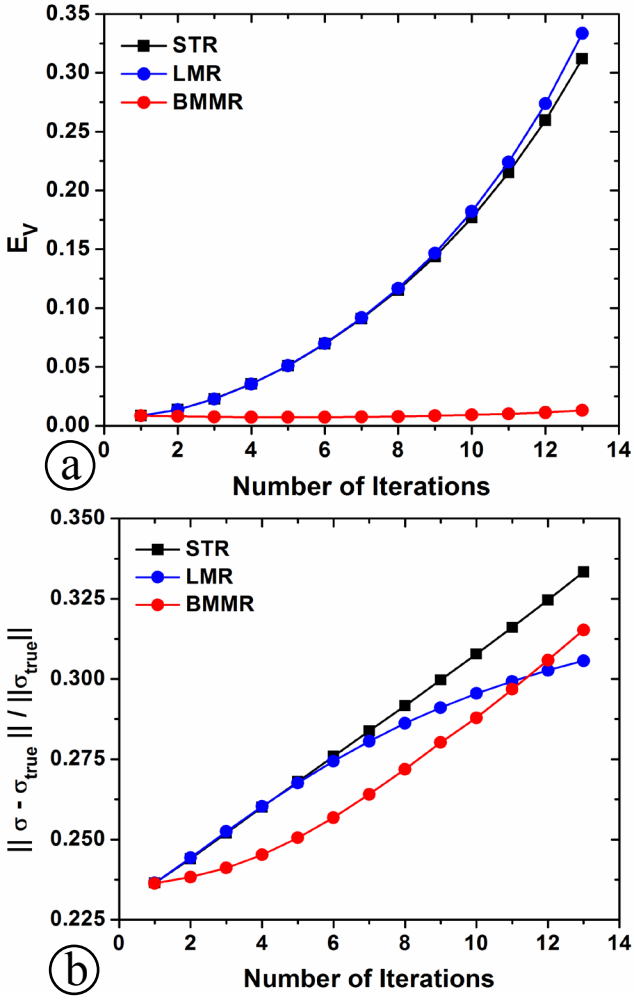


Fig.4: Error in different regularization methods for $\lambda = 0.01$: (a) normalized projection errors, (b) normalized solution error norm.

*Single Inhomogeneity Imaging*

Conductivity imaging of the phantoms with single inhomogeneity of different diameters at different positions shows that the BMMR technique gives better image reconstruction with less background noise. Reconstructed images obtained in STR, LMR and BMMR with $\lambda = 0.01$ show that, for the phantom with a circular inhomogeneity (D = 30 mm, L = 37.5 mm) near electrode No.-3 (Fig.-5a), the CNRs of the reconstructed images in STR (Fig.-5b) and LMR (Fig.-5c) methods are 1.91 and 2.07, respectively (Table-1). On the other hand, for the BMMR method (Fig.-5d), the CNR of the reconstructed image is 2.67 (Table-1). Results show that, for the same phantom, the PCRs of the reconstructed images with the STR and LMR methods are 37.35 % and 34.72 %, respectively, whereas it is 49.06 % for the BMMR method (Table-1). For the same reconstruction, it is also observed that the COCs of the reconstructed images with the STR and LMR methods are 1.52 and 1.49, respectively, whereas it is 2.14 in BMMR technique (Table-1). Results also show that $IC_{Mean}$ of the reconstructed images in the STR and LMR methods are 0.41 S/m and 0.40 S/m, respectively, whereas in the BMMR method it is 0.24 S/m (Table-1).

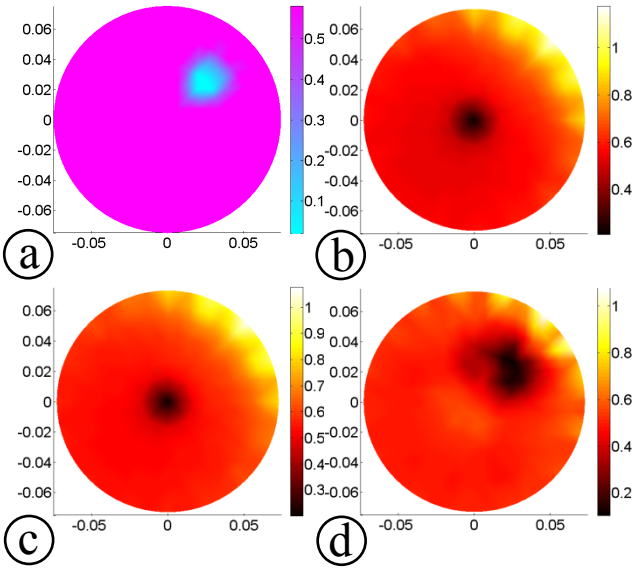


Fig.5: Conductivity reconstruction of the phantom with inhomogeneity (D = 30 mm, L = 37.5 mm) near electrode No.-3 ($\lambda = 0.01$): (a) original object, (b) image with STR, (c) image with LMR, (d) image with BMMR.

**Table-1:** CNR, PCR and COC of the conductivity images of Fig.-5

| $\lambda = 0.01$ | CNR | PCR | COC | $IC_{Mean}$ |
|---|---|---|---|---|
| **STR** | 1.91 | 37.35 | 1.52 | 0.41 |
| **LMR** | 2.07 | 34.72 | 1.49 | 0.40 |
| **BMMR** | 2.67 | 49.06 | 2.14 | 0.24 |

Conductivity imaging in STR, LMR and BMMR with $\lambda = 0.0001$ shows that, for the phantom with a circular inhomogeneity (D = 30 mm, L = 37.5 mm) near electrode No.-3 (Fig.-6a), the CNRs of the reconstructed images in the STR (Fig.-6b) and LMR (Fig.-6c) methods are 1.98 and 1.12, respectively (Table-2). On the other hand, for the BMMR method (Fig.-6d), the CNR of the reconstructed image is 2.67 (Table-2). Results show that, for the same

phantom, the PCRs of the reconstructed images with the STR and LMR methods are 46.30 % and 28.25 % respectively whereas it is 68.76 % for BMMR method (Table-2).

For the same reconstruction, it is also observed that the COCs of the reconstructed images with the STR and LMR methods are 2.05 and 1.46, respectively, whereas it is 4.60 in BMMR technique (Table-2). It is observed that $IC_{Mean}$ of the reconstructed images in the STR and LMR methods are 0.25 S/m and 0.34 S/m, respectively, whereas in the BMMR method it is 0.11 S/m (Table-2).

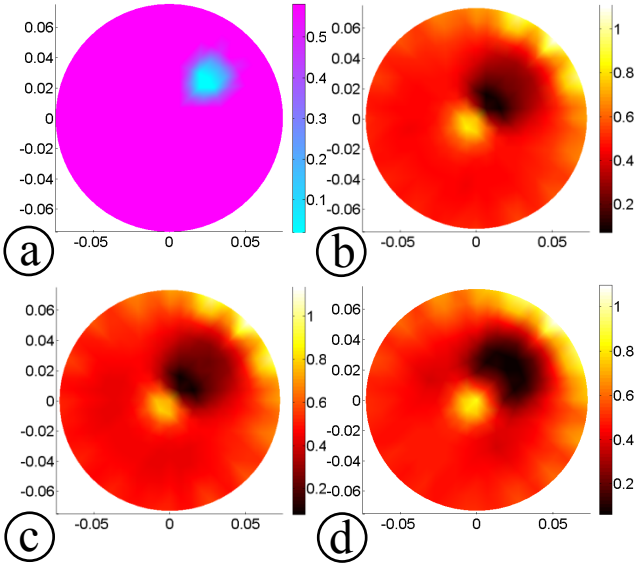


Fig.6: Conductivity reconstruction of the phantom with inhomogeneity (D = 30 mm, L = 37.5 mm) near electrode No.-3 (λ = 0.0001): (a) original object, (b) image with STR, (c) image with LMR, (d) image with BMMR.

**Table-2:** CNR, PCR and COC of the conductivity images of Fig.-6

| λ = 0.0001 | CNR | PCR | COC | $IC_{Mean}$ |
|---|---|---|---|---|
| **STR** | 1.98 | 46.30 | 2.05 | 0.25 |
| **LMR** | 1.12 | 28.25 | 1.46 | 0.34 |
| **BMMR** | 2.67 | 68.76 | 4.60 | 0.11 |

Conductivity imaging with λ = 0.00011 shows that, for the phantom with a circular inhomogeneity (D = 30 mm, L = 37.5 mm) near electrode No.-3 (Fig.-7a), the CNRs of the reconstructed images with the STR (Fig.-7b) and LMR (Fig.-7c) methods are 1.94 and 1.30, respectively, (Table-3) whereas in the BMMR method (Fig.-7d), it is 2.80 (Table-3).

Results show that, for the same phantom, the PCRs of the reconstructed images with the STR and LMR methods are 45.94 % and 38.46 %, respectively, whereas it is 68.02 for the BMMR method (Table-3).

It is also observed that the COCs of the reconstructed images with the STR and LMR methods are 2.04 and 1.81, respectively, whereas it is 4.20 in BMMR technique (Table-3). Results show that $IC_{Mean}$ of the reconstructed images in the STR and LMR methods are 0.25 S/m and 0.27 S/m, respectively, whereas in the BMMR method it is 0.12 S/m (Table-3). Hence, the conductivity reconstruction with different values of λ shows that the BMMR method improves the image quality compared to STR and LMR. Reconstruction with λ = 0.0001 gives a more clear aspects of the proposed method (BMMR) as the STR and LMR methods show the best result at λ = 0.0001.

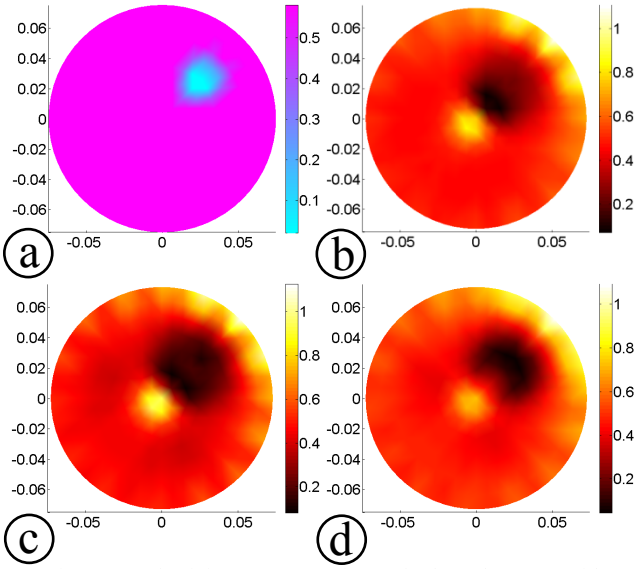


Fig.7: Conductivity reconstruction of the phantom with inhomogeneity (D = 30 mm, L = 37.5 mm) near electrode No.-3 (λ = 0.00011): (a) original object, (b) image with STR, (c) image with LMR, (d) image with BMMR.

**Table-3:** CNR, PCR and COC of the conductivity images of Fig.-7

| λ = 0.00011 | CNR | PCR | COC | $IC_{Mean}$ |
|---|---|---|---|---|
| **STR** | 1.94 | 45.94 | 2.04 | 0.25 |
| **LMR** | 1.30 | 38.46 | 1.81 | 0.27 |
| **BMMR** | 2.80 | 68.02 | 4.20 | 0.12 |

The conductivity imaging (with λ = 0.0001) of the phantoms with circular inhomogeneity of different diameters shows that the BMMR technique gives better image reconstruction with less background noise. Imaging (with λ = 0.0001) of the phantom with a circular inhomogeneity (D = 20 mm, L = 37.5 mm) near electrode. No.-3 (Fig.-8a) shows that the CNRs of the reconstructed images with the STR (Fig.-8b) and LMR (Fig.-8c) methods are 0.56 and 1.17, respectively (Table-4).

On the other hand, for the BMMR method (Fig.-8d), the CNR of the reconstructed image is 2.51 (Table-4). Results show that, for the same phantom, the PCRs of the reconstructed images with the STR and LMR methods are 12.73 % and 20.93 %, respectively, whereas it is 50.53 for the BMMR method (Table-4). In the same reconstruction, it is also observed that the COCs of the reconstructed images with the STR and LMR methods are 1.18 and 1.32, respectively, whereas it is 2.46 in BMMR technique (Table-4).

Imaging (with λ = 0.0001) of the phantom with a circular inhomogeneity (D = 30 mm, L = 37.5 mm) near electrode No.-3 (Fig.-9a) shows that the CNRs of the reconstructed images with the STR (Fig.-9b) and LMR (Fig.-9c) methods are 1.94 and 1.30, respectively, (Table-5) whereas in the BMMR method (Fig.-9d), it is 2.80 (Table-5).

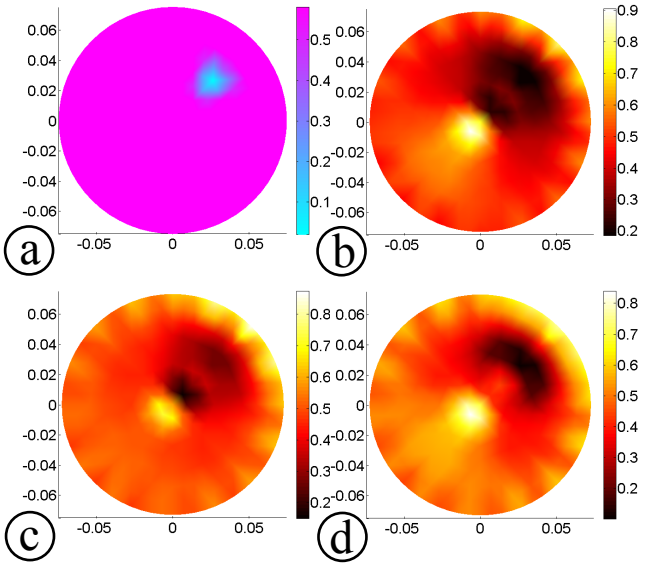


Fig.8: Conductivity reconstruction of the phantom with inhomogeneity (D = 20 mm, L = 37.5 mm) near electrode No.-3 (λ = 0.0001): (a) original object, (b) image with STR, (c) image with LMR, (d) image with BMMR.

**Table-4:** CNR, PCR and COC of the conductivity images of Fig.-8

| 20 mm Dia. | CNR | PCR | COC | $IC_{Mean}$ |
|---|---|---|---|---|
| STR | 0.56 | 12.73 | 1.18 | 0.40 |
| LMR | 1.17 | 20.93 | 1.32 | 0.37 |
| BMMR | 2.51 | 50.53 | 2.46 | 0.19 |

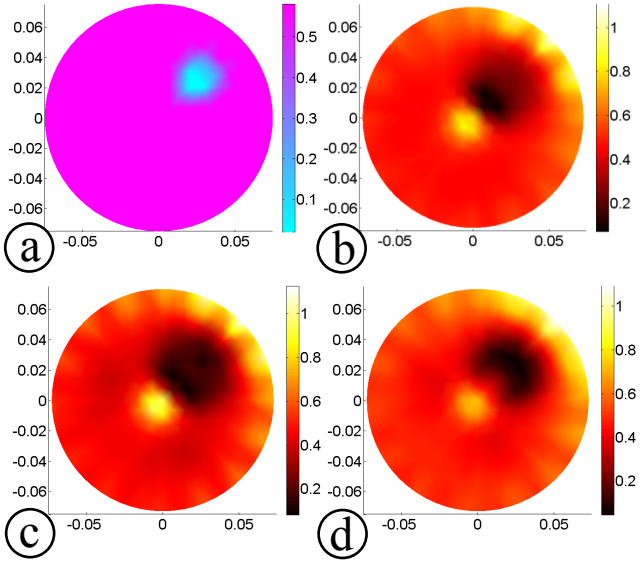


Fig.9: Conductivity reconstruction of the phantom with inhomogeneity (D = 30 mm, L = 37.5 mm) near electrode No.-3 (λ = 0.0001): (a) original object, (b) image with STR, (c) image with LMR, (d) image with BMMR.

Results show that, for the same phantom, the PCRs of the reconstructed images with the STR and LMR methods are 45.94 % and 38.46 %, respectively, whereas it is 68.02 % for the BMMR method (Table-5). It is also observed that the COCs of the reconstructed images with the STR and LMR methods are 2.04 and 1.81, respectively, whereas it is 4.20 in BMMR technique (Table-5).

**Table-5:** CNR, PCR and COC of the conductivity images of Fig.-9

| 30 mm Dia. | CNR | PCR | COC | $IC_{Mean}$ |
|---|---|---|---|---|
| STR | 1.94 | 45.94 | 2.04 | 0.25 |
| LMR | 1.30 | 38.46 | 1.81 | 0.27 |
| BMMR | 2.80 | 68.02 | 4.20 | 0.12 |

Conductivity reconstruction (with λ = 0.0001) shows that, for the phantom with a circular inhomogeneity (D = 40 mm, L = 37.5 mm) near electrode No.-3 (Fig.-10a), the CNRs of the reconstructed images with the STR (Fig.-10b) and LMR (Fig.-10c) methods are 1.91 and 2.14, respectively (Table-6). On the other hand, for the BMMR method (Fig.-10d), the CNR of the reconstructed image is 2.98 (Table-6). Results show that, for the same phantom, the PCRs of the reconstructed images with the STR and LMR methods are 53.07 % and 65.05 %, respectively, whereas it is 74.58 % for the BMMR method (Table-6). For the same reconstruction, it is also observed that the COCs of the reconstructed images with the STR and LMR methods are 2.29 and 3.33, respectively, whereas it is 5.06 in BMMR technique (Table-6).

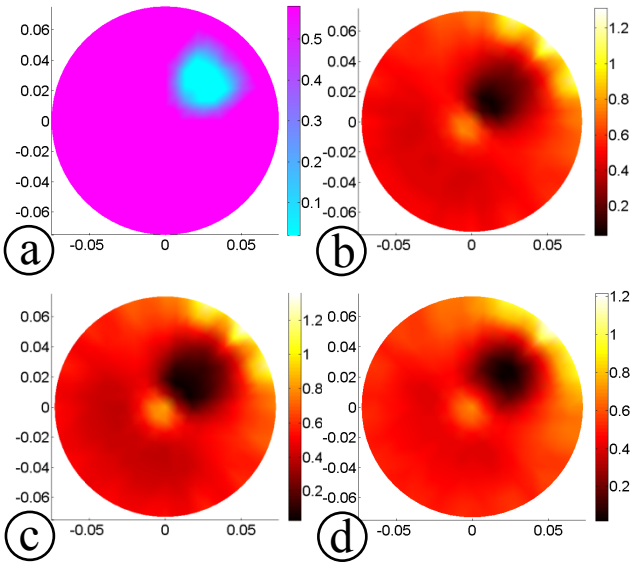


Fig.10: Conductivity reconstruction of the phantom with inhomogeneity (D = 40 mm, L = 37.5 mm) near electrode No.-3 (λ = 0.0001): (a) original object, (b) image with STR, (c) image with LMR, (d) image with BMMR.

**Table-6:** CNR, PCR and COC of the conductivity images of Fig.-10

| 40 mm Dia. | CNR | PCR | COC | $IC_{Mean}$ |
|---|---|---|---|---|
| STR | 1.91 | 53.07 | 2.29 | 0.23 |
| LMR | 2.14 | 65.05 | 3.33 | 0.16 |
| BMMR | 2.98 | 74.58 | 5.06 | 0.10 |

Conductivity imaging (with λ = 0.0001) of the phantoms with circular inhomogeneity at different positions also shows that the BMMR technique gives better image reconstruction with less background noise. Results show that, for the phantom with a circular inhomogeneity (D = 35 mm, L = 22.5 mm) near electrode. No.-3 (Fig.-11a), the CNRs of the reconstructed images with the STR (Fig.-11b) and LMR (Fig.-11c) methods are 2.22 and 1.86, respectively (Table-7). On the other hand, for the BMMR method (Fig.-11d), the CNR of the reconstructed image is 2.61 (Table-7). It is observed that, for the same phantom, the PCRs of the reconstructed images with the STR and LMR methods are 48.25 % and 44.09 %, respectively, whereas it is 55.67 for the BMMR method (Table-7). In the same reconstruction, it is also observed that the COCs of the reconstructed images with the STR and LMR methods are 1.72 and 1.60, respectively, whereas it is 2.04 in BMMR technique (Table-7).

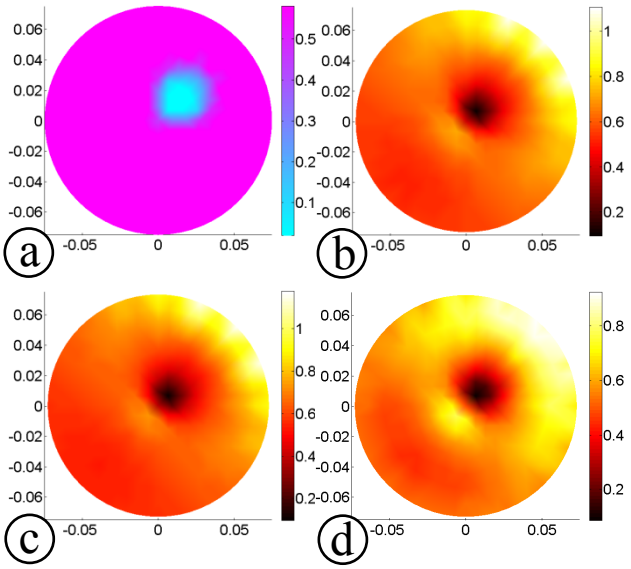


Fig.11: Conductivity reconstruction of the phantom with inhomogeneity (D = 35 mm, L = 22.5 mm) near electrode No.-3 (λ = 0.0001): (a) original object, (b) image with STR, (c) image with LMR, (d) image with BMMR.

**Table-7:** CNR, PCR and COC of the conductivity images of Fig.-11

| 22.5 mm Dist. | CNR | PCR | COC | $IC_{Mean}$ |
|---|---|---|---|---|
| **STR** | 2.22 | 48.25 | 1.72 | 0.38 |
| **LMR** | 1.86 | 44.09 | 1.60 | 0.41 |
| **BMMR** | 2.61 | 55.67 | 2.04 | 0.30 |

Imaging (with λ = 0.0001) of the phantom with a circular inhomogeneity (D = 35 mm, L = 37.5 mm) near electrode No.-3 (Fig.-12a) shows that the CNRs of the reconstructed images with the STR (Fig.- 12b) and LMR (Fig.- 12c) methods are 1.79 and 1.54, respectively, (Table-8) whereas in the BMMR method (Fig.- 12d), it is 2.75 (Table-8). Results show that, for the same phantom, the PCRs of the reconstructed images with the STR and LMR methods are 48.72 % and 45.90 %, respectively, whereas it is 75.33 for the BMMR method (Table-8). It is also observed that the COCs of the reconstructed images with the STR and LMR methods are 2.15 and 2.06, respectively, whereas it is 6.01 in BMMR technique (Table-8).

Reconstruction study (with λ = 0.0001) show that, for the phantom with a circular inhomogeneity (D = 35 mm, L = 52.5 mm) near electrode No.-3 (Fig.-13a), the CNRs of the reconstructed images with the STR (Fig.-13b) and LMR (Fig.-13c) methods are 3.44 and 3.57, respectively (Table-9). On the other hand, for the BMMR method (Fig.-13d), the CNR of the reconstructed image is 3.59 (Table-9).

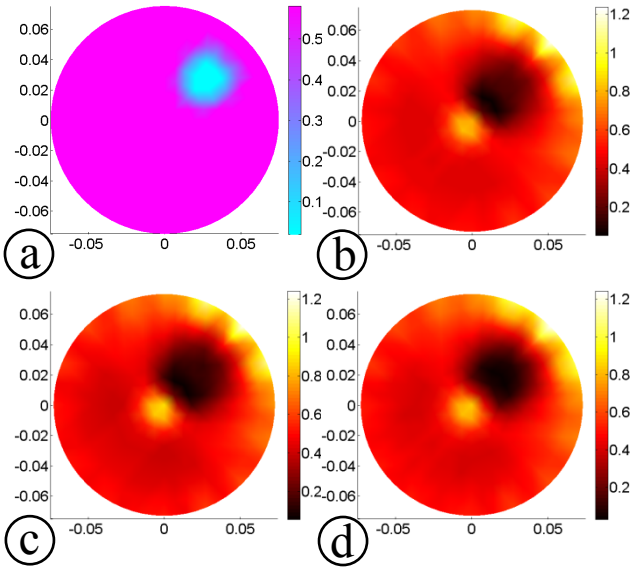


Fig.12: Conductivity reconstruction of the phantom with inhomogeneity (D = 35 mm, L = 37.5 mm) near electrode No.-3 (λ = 0.0001): (a) original object, (b) image with STR, (c) image with LMR, (d) image with BMMR.

**Table-8:** CNR, PCR and COC of the conductivity images of Fig.-12

| 37.5 mm Dist. | CNR | PCR | COC | $IC_{Mean}$ |
|---|---|---|---|---|
| **STR** | 1.79 | 48.72 | 2.15 | 0.24 |
| **LMR** | 1.54 | 45.90 | 2.06 | 0.24 |
| **BMMR** | 2.75 | 75.33 | 6.01 | 0.08 |

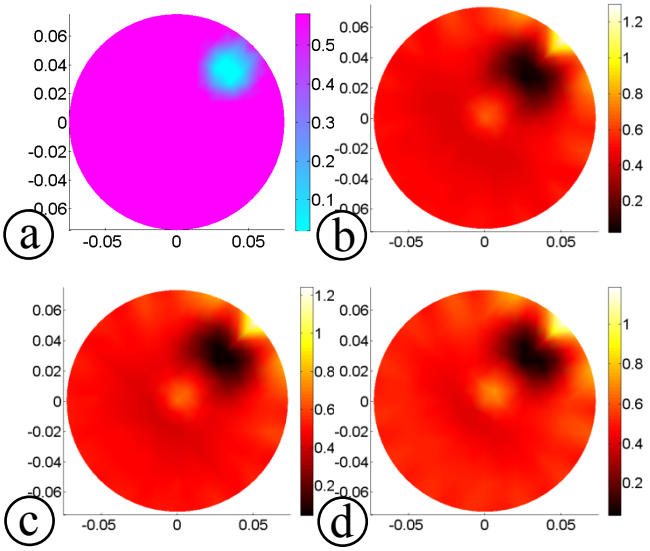


Fig.13: Conductivity reconstruction of the phantom with inhomogeneity (D = 35 mm, L = 52.5 mm) near electrode No.-3 (λ = 0.0001): (a) original object, (b) image with STR, (c) image with LMR, (d) image with BMMR.

Results show that, for the same phantom, the PCRs of the reconstructed images with the STR and LMR methods are 63.75 % and 62.77 %, respectively, whereas it is 63.77 % for the BMMR method (Table-9). For the same reconstruction, it is also observed that the COCs of the reconstructed images with the STR and LMR methods are 3.70 and 3.54, respectively, whereas it is 3.50 in BMMR technique (Table-9).

**Table-9:** CNR, PCR and COC of the conductivity images of Fig.-13

| 52.5 mm Dist. | CNR | PCR | COC | $IC_{Mean}$ |
|---|---|---|---|---|
| **STR** | 3.44 | 63.75 | 3.70 | 0.13 |
| **LMR** | 3.57 | 62.77 | 3.54 | 0.14 |
| **BMMR** | 3.59 | 63.77 | 3.50 | 0.14 |

*Multiple Inhomogeneity Imaging*

Conductivity reconstruction studies show that, for multiple inhomogeneity phantoms, the MoBIIR algorithm re-constructs better conductivity images with BMMR technique. As it is observed that, for the STR and LMR methods, $E_V$ is minimum at $\lambda = 0.0001$ and for the BMMR method $E_V$ becomes minimum at $\lambda = 0.01$, the multiple object imaging is also conducted for these two values of $\lambda$. For further study, the conductivity reconstruction is also conducted with a intermediate value of $\lambda$ (with $\lambda = 0.00011$ and $\lambda = 0.0011$).

Conductivity imaging (with $\lambda = 0.0001$) of the phantoms with double inhomogeneity shows that the BMMR technique gives better image reconstruction with less background noise.

Result shows that, for the phantom with a double inhomogeneity (D = 40 mm, L = 37.5 mm) near electrode No.-3 and 15 (Fig.-14a), the quality of the reconstructed images with the STR (Fig.-14b) and LMR (Fig.-14c) methods are poor compared to the BMMR method (Fig.-14d).

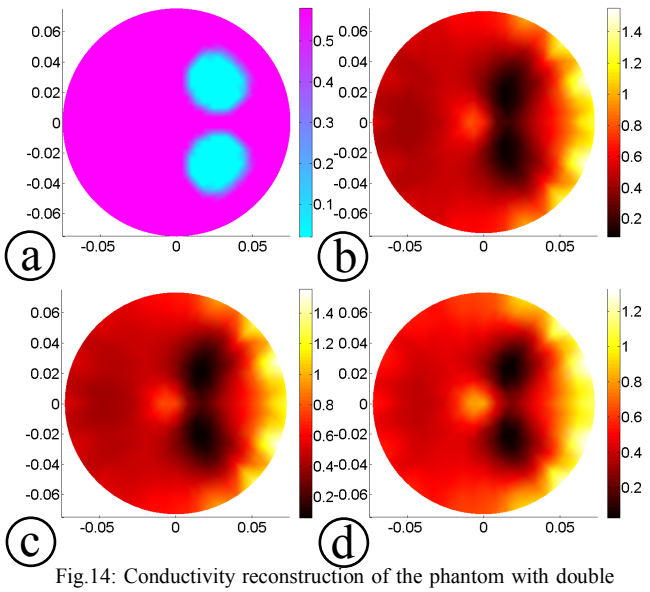


Fig.14: Conductivity reconstruction of the phantom with double inhomogeneity (D = 40 mm, L = 37.5 mm) near electrode No.-3 and 15 ($\lambda = 0.0001$): (a) original object, (b) image with STR, (c) image with LMR, (d) image with BMMR.

It is observed that there is more background noise in STR and LMR. On the other hand the background noise is reduced in conductivity images obtained in BMMR technique. Results also show that the inhomogeneities are not separately reconstructed with their own shape in the STR and LMR method whereas in BMMR technique both the inhomogeneities are reconstructed with better resolution.

Conductivity imaging (with $\lambda = 0.01$) of the phantoms with a double inhomogeneity (D = 40 mm, L = 52.5 mm) near electrode No.-3 and 15 (Fig.-15a) shows that the quality of the reconstructed images with the STR (Fig.-15b) and LMR (Fig.-15c) methods are poor compared to the image obtained with the BMMR method (Fig.-15d).

It is also observed that the background noise is reduced in conductivity images in BMMR technique. On the other hand there is more background noise in STR and LMR. Results also show that the inhomogeneities are not separately reconstructed with their proper shape in the STR and LMR methods whereas in BMMR technique both the inhomogeneities are reconstructed with better resolution.

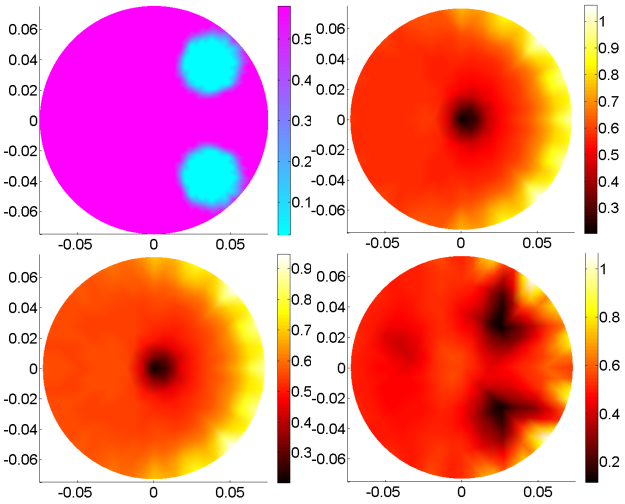

Fig.15: Conductivity reconstruction of the phantom with double inhomogeneity (D = 40 mm, L = 52.5 mm) near electrode No.-3 and 15 ($\lambda = 0.01$): (a) original object, (b) image with STR, (c) image with LMR, (d) image with BMMR.

Conductivity imaging with $\lambda = 0.0011$ shows that, for the phantom with two inhomogeneities (D = 40 mm, L = 50.0 mm) near electrode No.-3 and 7 (Fig.-16a), conductivity images are not clear in the STR (Fig.-16b) and LMR (Fig.-16c) method whereas the images are very clear in the BMMR method (Fig.-16d).

It is observed that there is more background noise in STR and LMR. On the other hand the background noise is reduced in conductivity images in BMMR technique. Results also show that the inhomogeneities are not separately reconstructed with their own shape in the STR and LMR method whereas in BMMR technique both the inhomogeneities are reconstructed with better resolution.

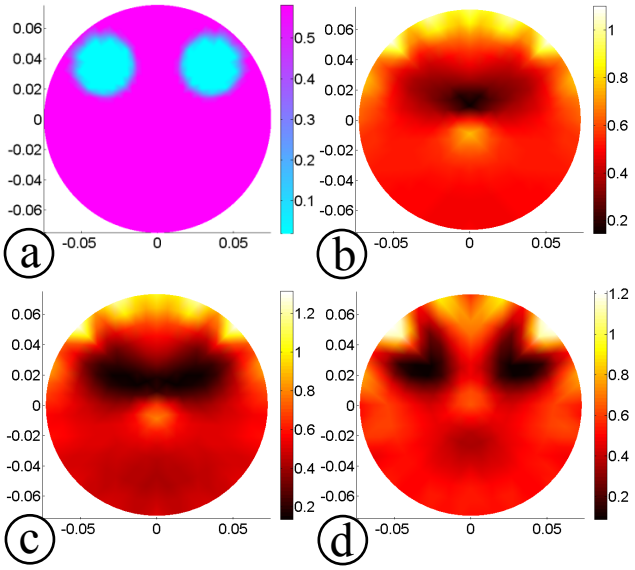


Fig.16: Conductivity reconstruction of the phantom with double inhomogeneity (D = 40 mm, L = 50.0 mm) near electrode No.-3 and 7 (λ = 0.0011): (a) original object, (b) image with STR, (c) image with LMR, (d) image with BMMR.

On the other hand, in conductivity imaging (with λ = 0.0011) of the phantom with two inhomogeneities (D = 40 mm, L = 37.5 mm) near the phantom center (Fig.-17a), the STR and LMR method fail to reconstruct the images of two separate objects (Fig.-17b-17c) whereas the reconstructed images are very clear in the BMMR method (Fig.-17d). Results also show that the inhomogeneities are not separately reconstructed with their own shape in the STR and LMR methods whereas in BMMR technique both the inhomogeneities are reconstructed with better resolution.

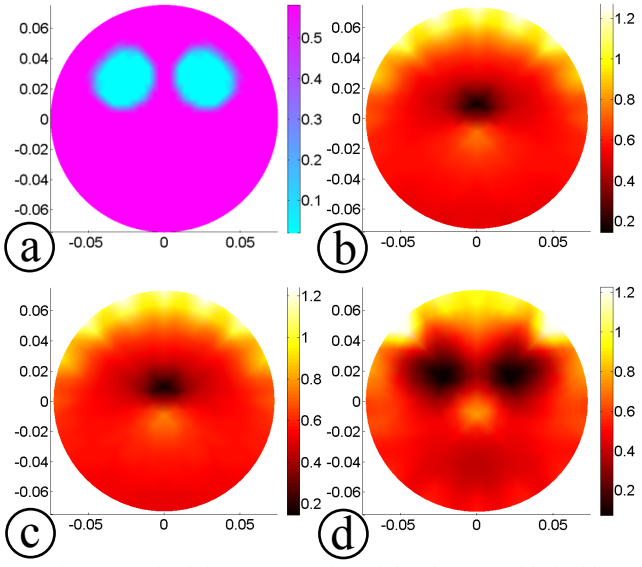


Fig.17: Conductivity reconstruction of the phantom with double inhomogeneity (D = 40 mm, L = 37.5 mm) near electrode No.-3 and 7 (λ = 0.0011): (a) original object, (b) image with STR, (c) image with LMR, (d) image with BMMR.

Conductivity imaging of the phantoms with three inhomogeneities also shows that the BMMR technique gives better image reconstruction with less background noise compared to the STR and LMR methods. Conductivity imaging (with λ = 0.0001) of a phantom (Fig.-18a) with triple inhomogeneity (D = 40 mm, L = 37.5 mm) shows that the STR and LMR methods reconstruct the images of all the three objects with a lot of image blurring and unwanted noise (Fig.-18b and 18c) whereas all the three objects are reconstructed with less image blurring in the BMMR method (Fig.-18d). It is also observed that there is more background noise in STR and LMR. On the other hand the background noise is reduced in BMMR technique. Results also show that the inhomogeneities are not separately reconstructed with their own shape in the STR and LMR method whereas in BMMR technique both the objects are reconstructed with better resolution.

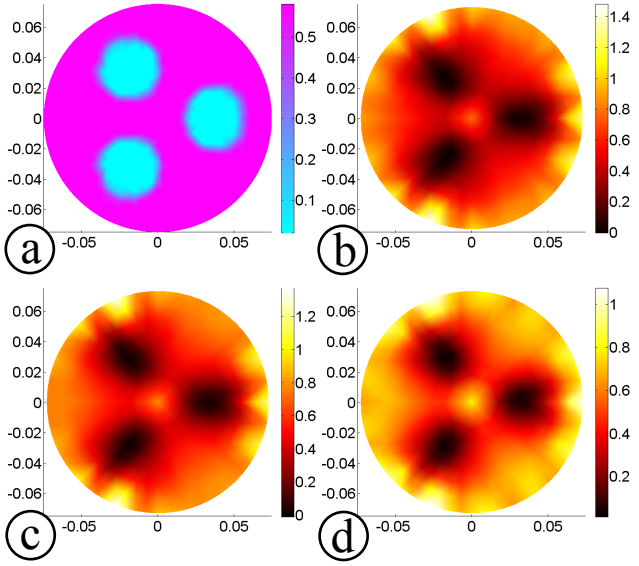


Fig.18: Conductivity reconstruction of the phantom with tripple inhomogeneity (D = 40 mm, L = 37.5 mm) near electrode No.-1, between electrode No.-6-7 and between electrode No.-11-12 (λ = 0.0001): (a) original object, (b) image with STR, (c) image with LMR, (d) image with BMMR

It is also observed that, for the image reconstruction (with λ = 0.0011) of the phantom with three objects (D = 40 mm, L = 50 mm) near the phantom boundary (Fig.-19a), conductivity images are not properly reconstructed in the STR (Fig.-19b) and LMR (Fig.-19c) method whereas the images are very clear in the BMMR method (Fig.-19d). It is observed that there is more background noise in STR and LMR. On the other hand the background noise is reduced in conductivity images in BMMR technique. Results also show that the inhomogeneities are not separately reconstructed with their own shape in the STR and LMR method whereas in BMMR technique both the inhomogeneities are reconstructed with better resolution.

On the other hand, for a triple inhomogeneity (D = 40 mm, L = 37.5 mm) phantom with objects near the phantom center (Fig.-20a), conductivity imaging (with λ = 0.0011) shows that the STR and LMR methods reconstruct very poor quality images of all the three separate objects (Fig.-20b and 20c ) whereas the three objects are successfully reconstructed in the BMMR method (Fig.-20d). It is also

observed that the background noise is reduced in conductivity images in BMMR technique. On the other hand, there is more background noise in STR and LMR. Results also show that the inhomogeneities are not separately reconstructed with their own shape in the STR and LMR method whereas in BMMR technique both the objects are reconstructed with better resolution.

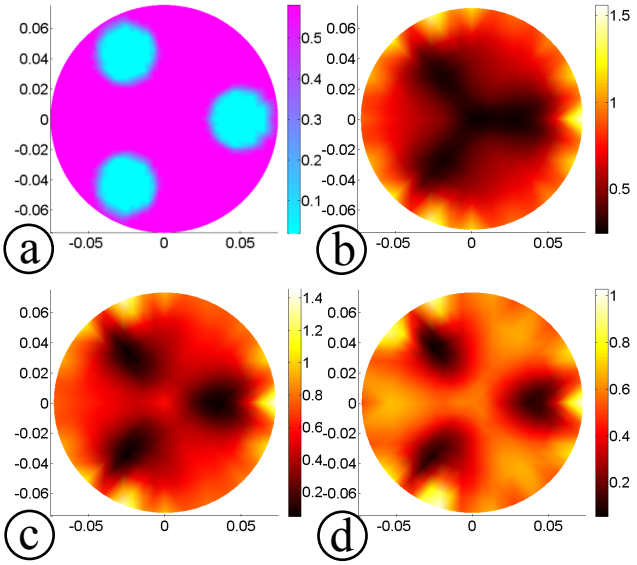


Fig.19: Conductivity reconstruction of the phantom with tripple inhomogeneity (D = 40 mm, L = 50.0 mm) near electrode No.-1, between electrode No.-6-7 and between electrode No.-11-12 (λ = 0.0011): (a) original object, (b) image with STR, (c) image with LMR, (d) image with BMMR.

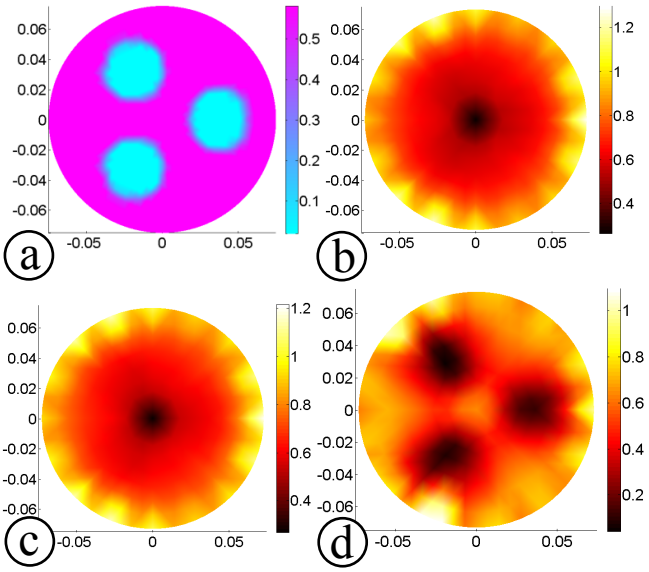


Fig.20: Conductivity reconstruction of the phantom with tripple inhomogeneity (D = 40 mm, L = 37.5 mm) near electrode No.-1, between electrode No.-6-7 and between electrode No.-11-12 (λ = 0.0011): (a) original object, (b) image with STR, (c) image with LMR, (d) image with BMMR

A reconstruction study (with λ = 0.00011) shows that, for the phantom with three objects (D = 40 mm, L = 37.5 mm) near the center (Fig.-21a) which is identical to the phantom of the previous study (Fig.-20a), conductivity images are improved when the regularization parameter **λ** is reduced to 0.00011 in the STR (Fig.-21b) and LMR (Fig.-21c) methods. But the image obtained in BMMR technique (Fig.-21d) is still found better compared to the STR and LMR methods. Results also show that the inhomogeneities are not separately reconstructed with their proper shape in the STR and LMR methods whereas in BMMR technique both the inhomogeneities are reconstructed with better resolution.

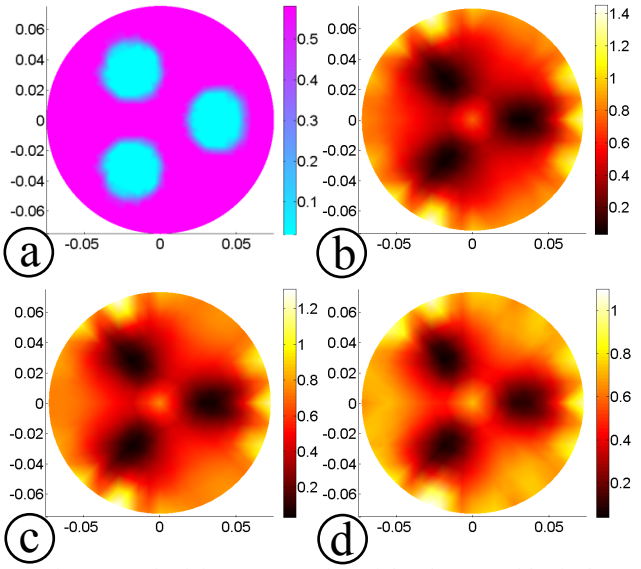


Fig.21: Conductivity reconstruction of the phantom with tripple inhomogeneity (D = 40 mm, L = 37.5 mm) near electrode No.-1, between electrode No.-6-7 and between electrode No.-11-12 (λ = 0.00011): (a) original object, (b) image with STR, (c) image with LMR, (d) image with BMMR

Image reconstruction (with λ = 0.00011) shows that for the phantom with three objects near the phantom center (D = 40 mm, L = 30 mm) (Fig.-22a), conductivity images are very poor in the STR (Fig.- 22b) and LMR (Fig.- 22c) methods. But the reconstructed image is remarkably improved in BMMR technique (Fig.- 22d) with the same **λ**.

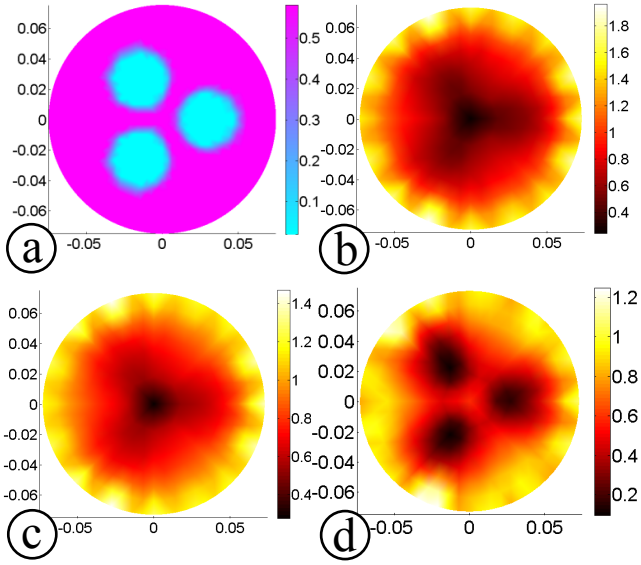


Fig.22: Conductivity reconstruction of the phantom with tripple inhomogeneity (D = 40 mm, L = 30.0 mm) near electrode No.-1, between electrode No.-6-7 and between electrode No.-11-12 (λ = 0.00011): (a) original object, (b) image with STR, (c) image with LMR, (d) image with BMMR

## Discussion

Reconstructed image quality greatly depends on the Jacobian matrix (J), response matrix ($J^TJ$) and regularization parameter ($\lambda$) of reconstruction algorithm in Electrical Impedance Tomography. In the MoBIIR algorithm with STR regularization, the highest value of $J^TJ$ is chosen as $\eta$ to calculate $\lambda$ ($\lambda_r = \lambda*\eta$). On the other hand, in the LMR method, $\lambda_r$ is calculated as $\lambda_r = \lambda*\eta$ (where $\eta$ is the highest value of the response matrix $J^TJ$) in the first iteration and then it is reduced by a factor of $\sqrt{10}$ as iteration continues. Hence, in both the STR and LMR methods, a constant regularization parameter is obtained at each iteration and as a result the local or regional physiological attributes are not taken into account in them. Furthermore, due to the addition of a constant regularization parameter to the matrix $J^TJ$, it perturbs the original system of equations and these perturbations are not based on the spectral information. Hence this perturbation may introduce a significant error in the solution as well as some unwanted solution could be obtained. In this paper a Block Matrix based Multiple Regularization (BMMR) technique is proposed in which the response matrix ($J^TJ$) has been partitioned into several sub-block matrices and the largest element of each sub-block matrix has been chosen as a regularization parameter for the nodes contained by that sub-block. A symmetric finite element mesh containing 512 triangular elements and 289 nodes is used in the MoBIIR algorithm both for the forward and inverse solution of the image reconstruction process. Conductivity images of different phantom geometries are reconstructed in MoBIIR with STR, LMR and BMMR techniques using different regularization parameters. Simulated boundary data are generated for single and multiple inhomogeneity phantoms and the conductivity images reconstructed with BMMR technique. Reconstruction results obtained in the BMMR method for different regularization parameters are compared with the STR and LMR methods. All the images are analyzed with their normalized error terms and image contrast parameters defined by their elemental conductivity profiles. It is observed that the normalized projection errors in STR and LMR becomes minimum at $\lambda = 0.0001$ and $\lambda = 0.0001$, respectively. On the other hand, in the BMMR method the $E_V$ becomes minimum at $\lambda = 0.01$. Conductivity reconstructions also show that the $E_V$ and the $E_\sigma$ in STR and LMR are larger than in the BMMR technique. Imaging with $\lambda = 0.0001$ in all the methods (STR, LMR and BMMR) gives a more clear aspects of the proposed method (BMMR) as the STR and LMR methods show the best results at $\lambda = 0.0001$. Conductivity reconstruction is studied in detail with the simulated boundary data obtained from the phantoms with single and multiple inhomogeneity of different diameters and different geometric positions. To compare the image reconstruction and image quality in the STR, LMR and BMMR methods, the conductivity reconstruction is conducted first with $\lambda = 0.01$ and then with $\lambda = 0.0001$. For further studies, the conductivity imaging is also studied using the STR, LMR and BMMR method with some intermediate values of $\lambda$ (with $\lambda = 0.0011$ and $\lambda = 0.00011$). It is observed that the impedance images are improved in BMMR, not only with all the phantom configurations, but also for all the values of $\lambda$ used in the present study. Results also show that the CNR, PCR and COC are found high in BMMR technique. It is observed that the $IC_{Mean}$ of all the conductivity images are improved with the BMMR method. Hence, it is concluded that the proposed BMMR technique reduces the projection errors and solution error and provides improved image reconstruction in EIT with better image quality and improved image resolution.

## Conclusions

A Block Matrix based Multiple Regularization (BMMR) technique is proposed for improving image reconstruction in Electrical Impedance Tomography (EIT). Conductivity images are reconstructed from the simulated boundary data in MoBIIR algorithm with BMMR method and results are compared with the STR and LMR methods. Conductivity imaging studies show that the BMMR technique improves the impedance image quality and its spatial resolution for single and multiple inhomogeneity phantoms of different geometries. It is also observed that the BMMR technique reduces the projection error as well as the solution error and improves the conductivity reconstruction in EIT. Results show that the BMMR method improves the reconstructed image quality and increases the inhomogeneity conductivity profile by reducing background noise for all the phantom configurations. CNR, PCR, COC and $IC_{Mean}$ are improved in BMMR technique compared to the STR and LMR methods. Hence it is concluded that the reconstructed image quality and image resolution can be enhanced with BMMR technique for conductivity imaging in EIT.

## References


1. Webster JG, Electrical impedance tomography. Adam Hilger Series of Biomedical Engineering, Adam Hilger, New York, USA 1990.
2. Cheney M, David Isaacson, Jonathan C. Newell. Electrical Impedance Tomography. SIAM Review, 41(1), 85–101, 1999. doi:10.1137/S0036144598333613
3. Bayford RH. Bioimpedance Tomography (Electrical Impedance Tomography). Annual Review of Biomedical Engineering, 8, 63-91, 2006. doi:10.1146/annurev.bioeng.8.061505.095716
4. Denyer CWL, Electronics for Real-Time and Three-Dimensional Electrical Impedance Tomographs, PhD Thesis, Oxford Brookes University, 1996
5. Chen Z, Brown EN and Barbieri R. Assessment of Autonomic Control and Respiratory Sinus Arrhythmia Using Point Process Models of Human Heart Beat Dynamics. IEEE Transactions on Electromagnetic Compatibility, 56(7), 1791-1802, 2009.

6. Fabrizi L, McEwan A, Oh T, Woo EJ, Holder DS. An electrode addressing protocol for imaging brain function with electrical impedance tomography using a 16-channel semi-parallel system. Physiol. Meas., 30, S85–S101, 2009. doi:10.1088/0967-3334/30/6/S06
7. Bagshaw AP, Liston AD, Bayford RH, Tizzard A, Gibson AP, Tidswell AT, Sparkes MK, Dehghani H, Binnie CD and Holder DS. Electrical impedance tomography of human brain function using reconstruction algorithms based on the finite element method. NeuroImage 20, 752–764, 2003. doi:10.1016/S1053-8119(03)00301-X
8. Murphy D, Burton P, Coombs R, Tarassenko L and Rolfe P. Impedance Imaging in the Newborn. Clin. Phys. Physiol. Meas., 8, Suppl. A, 131-40, 1987.
9. Hinz J, Neumann P, Dudykevych T, Andersson LG, Wrigge H, Burchardi H, and Hedenstierna G. Regional Ventilation by Electrical Impedance Tomography: A Comparison With Ventilation Scintigraphy in Pigs. Chest, 124, 314–322, 2003. doi:10.1378/chest.124.1.314
10. Noordegraaf AV, Faes TJC, Janse A, Marcus JT, Heethaar RM, Postmus PE and de Vries PMJM. Improvement of cardiac imaging in electrical impedance tomography by means of a new electrode configuration. Physiol. Meas., 17, 179–188, 1996. doi:10.1088/0967-3334/17/3/004
11. Hope TA and Iles SE. Technology review: The use of electrical impedance scanning in the detection of breast cancer. Breast Cancer Res., 6, 69-74, 2004. doi:10.1186/bcr744
12. Dickin F and Wang M. Electrical resistance tomography for process applications. Meas. Sci. and Technol., 7, 247, 1996. doi:10.1088/0957-0233/7/3/005
13. Stephensona DR, Rodgersa TL, Manna R and York TA. Application of Three-Dimensional Electrical Impedance Tomography to Investigate Fluid Mixing in a Stirred Vessel. 13th European Conference on Mixing, London, 14-17 April 2009.
14. Kotre CJ. Subsurface electrical impedance imaging: measurement strategy, image reconstruction and in vivo results. Physiol. Meas., 17, A197–A204, 1996. doi:10.1088/0967-3334/17/4A/024
15. Linderholm P, Marescot L, Loke MH, and Renaud P. Cell Culture Imaging Using Microimpedance Tomography. IEEE Transactions on Biomedical Engineering, 55(1), 138-146, 2008. doi:10.1109/TBME.2007.910649
16. Denyer CWL. Electronics for real-time and three-dimensional electrical impedance tomographs. PhD Thesis Oxford Brookes University, January 1996.
17. Huang CN, Yu FM and Chung HY. The Scanning Data Collection Strategy for Enhancing the Quality of Electrical Impedance Tomography. IEEE Transactions on Instrumentation And Measurement, 57(6), 1193-1198, 2008. doi:10.1109/TIM.2007.915149
18. Metherall P. Three Dimensional Electrical Impedance Tomography of the Human Thorax. PhD Thesis, University of Sheffield, January 1998.
19. Brown BH. Medical impedance tomography and process impedance tomography: a brief review. Measurement Science & Technology, 12, 991-996, 2001. doi:10.1088/0957-0233/12/8/301
20. Hou WD, and Mo YL. Increasing image resolution in electrical impedance tomography. Electronics Letters, 38, 701-702, 2002. doi:10.1049/el:20020477
21. Bera TK and Nagaraju J. Studying the Boundary Data Profile of A Practical Phantom for Medical Electrical Impedance Tomography with Different Electrode Geometries. Proceedings of The World Congress on Medical Physics and Biomedical Engineering-2009 Sept 7–12, 2009, Munich, Germany, IFMBE Proceedings 25/II, pp. 925–929. doi:10.1007/978-3-642-03879-2_258
22. Bera TK and Nagaraju J. A Stainless Steel Electrode Phantom to Study the Forward Problem of Electrical Impedance Tomography (EIT). Sensors & Transducers Journal, 104(5), 33-40, 2009.
23. Bera TK and Nagaraju J. A Simple Instrumentation Calibration Technique for Electrical Impedance Tomography (EIT) Using A 16 Electrode Phantom. Proceedings of The Fifth Annual IEEE Conference on Automation Science and Engineering (IEEE CASE 2009), Bangalore, August 22 to 25, pp. 347-352. doi:10.1109/COASE.2009.5234117
24. Holder DS, Hanquan Y and Rao A. Some practical biological phantoms for calibrating multifrequency electrical impedance tomography. Physiol. Meas., 17, A167-A177, 1996. doi:10.1088/0967-3334/17/4A/021
25. Bera TK and Nagaraju J. Resistivity Imaging of a Reconfigurable Phantom With Circular Inhomogeneities in 2D-Electrical Impedance Tomography. Measurement, 44(3), 518-526, 2011. doi:10.1016/j.measurement.2010.11.015
26. Bera TK and Nagaraju J. A Reconfigurable Practical Phantom for Studying the 2 D Electrical Impedance Tomography (EIT) Using a FEM Based Forward Solver, 10th International Conference on Biomedical Applications of Electrical Impedance Tomography (EIT 2009), School of Mathematics, The University of Manchester, UK, 16th-19th June 2009.
27. Lionheart WRB. EIT reconstruction algorithms: pitfalls, challenges and recent developments. Physiol. Meas., 25, 125–142, 2004. doi:10.1088/0967-3334/25/1/021
28. Kolehmainen V, Vauhkonen M, Karjalainen PA, Kaipio JP. Assessment of errors in static electrical impedance tomography with adjacent and trigonometric current patterns. Physiol Meas. 18(4), 289-303, 1997. doi:10.1088/0967-3334/18/4/003
29. Bera TK and Nagaraju J. A Study of Practical Biological Phantoms with Simple Instrumentation for Electrical Impedance Tomography (EIT). Proceedings of IEEE International Instrumentation and Measurement Technology Conference (I2MTC2009), Singapore, 5th - 7th May 2009, pp 511-516. doi:10.1109/IMTC.2009.5168503
30. Riu PJ, Rosell J, Lozano A and Pallà-Areny R. Multi-frequency static imaging in electrical impedance tomography: Part 1 instrumentation requirements. Med. Biol. Eng. Comput., 33(6), 784-792, 1995. doi:10.1007/BF02523010
31. Bera TK and Nagaraju J. A Multifrequency Constant Current Source for Medical Electrical Impedance Tomography. Proceedings of the IEEE International Conference on Systems in Medicine and Biology 2010 (IEEE ICSMB 2010), 16th-18th Dec'2010, Kharagpur, India, pp-290-295. doi: 10.1109/ICSMB.2010.5735387
32. Loh WW, Pinheiro PAT, Dickin FJ and Waterfall RC. Low common mode error data collection strategy for electrical resistance tomography. Electronics Letters, 34(15), 1998. doi:10.1049/el:19980846
33. Bushberg JT, Seibert JA, Leidholdt Jr. EM and Boone JM. The Essential Physics of Medical Imaging. Lippincott Williams & Wilkins; 2nd edition, 2001.

34. Kim MC, Kim S, Kim KY and Lee YJ. Regularization Methods in Electrical Impedance Tomography Technique for The Two-Phase Flow Visualization. Int. Comm. Heat Mass Transfer, 28(6), 173-782, 2001. doi:10.1016/S0735-1933(01)00281-0

35. Soleimani M and Lionheart WRB. Nonlinear image reconstruction in electrical capacitance tomography using experimental data. Meas. Sci. Technol., 16(10), 1987–1996, 2005. doi:10.1088/0957-0233/16/10/014

36. Niu H., Guo P., Ji L., Zhao Q. and Jiang T. Improving image quality of diffuse optical tomography with a projection-error-based adaptive regularization method. Optics Express, 16(17), 12423, 2008. doi:10.1364/OE.16.012423

37. Biswas SK, Rajan K, Vasu RM. Regional sub-block matrices based multiple regularization and biomedical image reconstruction. Systems in Medicine and Biology (ICSMB), 2010 International Conference on, 16-18 Dec. 2010, pp 61 - 66.

38. Biswas SK, Rajan K, Vasu RM. Diffuse optical tomographic imager using a single light source. J. Appl. Phys., 105(2), 024702, 2009. doi:10.1063/1.3040016

39. Yorkey TJ. Comparing reconstruction methods for electrical impedance tomography, PhD thesis, University of. Wisconsin at Madison, Madison, WI 53706, 1986.

40. Holder DS. Electrical impedance tomography: methods, history and applications. (Series in Medical Physics and Biomedical Engineering), Institute of Physics Publishing Ltd., 2005.

41. Grootveld CJ. Measuring and Modeling of Concentrated Settling Suspensions Using Electrical Impedance Tomography. PhD Thesis, Delft University of Technology, The Netherlands, 1996.

42. Adler A, Guardo R. Electrical impedance tomography: regularized imaging and contrast detection. IEEE Trans. Med Imag., 15(2), 170- 179, 1996. doi:10.1109/42.491418

43. Pogue BW, Willscher C, McBride TO, Osterberg UL, and Paulsen KD. Contrast-detail analysis for detection and characterization with near-infrared diffuse tomography. Med. Phys., 27, 2693-2700, 2000. doi:10.1118/1.1323984

44. Bera TK and Nagaraju J. A FEM-Based Forward Solver for Studying the Forward Problem of Electrical Impedance Tomography (EIT) with A Practical Biological Phantom. Proceedings of IEEE International Advance Computing Conference' 2009 (IEEE IACC - 2009), 6-7th March 2009, Patiala, Punjab, India, pp 1375 - 1381. doi:10.1109/IADCC.2009.4809217

45. Reddy JN. An Introduction to the Finite Element Method. 3rd Ed., 2nd Reprint, TATA McGraw-Hill Pub. Co. Ltd, 2006.

46. Graham BM. Enhancements in Electrical Impedance Tomography (EIT) Image Reconstruction for 3D Lung Imaging. PhD thesis, University of Ottawa, April 2007.

47. Arridge SR. Optical tomography in medical imaging. Inverse Problems, 15, R41–R93, 1999. doi:10.1088/0266-5611/15/2/022

48. Bera TK, Biswas SK, Rajan K and Nagaraju J. Improving Image Quality in Electrical Impedance Tomography (EIT) Using Projection Error Propagation-Based Regularization (PEPR) Technique: A Simulation Study. Journal of Electrical Bioimpedance, 2, 2–12, 2011. doi:10.5617/jeb.158